

# NUMERICAL EVALUATION FOR FAN-NOISE SHIELDING EFFECTS ON AFT-FUSELAGE MOUNTED AND EMBEDDED ENGINES

Tomoaki Ikeda<sup>1</sup>, Ryutaro Furuya<sup>2</sup> & Mitsuhiro Murayama<sup>1</sup>

<sup>1</sup>Japan Aerospace Exploration Agency (JAXA), 7-44-1 Jindaiji-Higashi, Chofu, Tokyo 182-8522, Japan <sup>2</sup>Ryoyu Systems Co., Ltd., 6-19 Ohe-cho, Minato-ku, Nagoya 455-0024, Japan

#### **Abstract**

Engine fan-noise propagation is computationally investigated for a midsize, fuel-efficient and low-noise conceptual aircraft model in a takeoff flight condition. In its baseline design, two engine nacelles are mounted with pylons on aft-fuselage. The boundary layer ingestion (BLI) model is also tested to examine its noise shielding efficiency. Acoustic propagation is volumetrically solved at 2500Hz considering a local convection effect. Although both designs successfully lower the perceived noise level at ground, the BLI model shows better noise shielding capability, clearly captured on a far-field noise sphere as well.

Keywords: Computational Aeroacoustics, Noise Shielding, Boundary Layer Ingestion

## 1. Introduction

Due to growing environmental awareness in recent years, technological innovations to reduce environmental impacts are in great demand in the development of commercial aircraft for next generation. Low-carbon technologies to constrain carbon dioxide emissions, as well as noise reduction research toward upcoming regulations on more stringent noise emission control, are our urgent tasks these days. Many elemental studies have been conducted to reduce fuel consumption, such as the drag reduction study for better aerodynamic designs, or the improvement of propulsion fuel efficiency. As an environmentally conscious design regarding propulsion system, the boundary-layer ingestion (BLI) technique can be a prospective candidate. BLI is the integration technique of an aircraft propulsion system to reduce overall fuel consumption. Engine nacelles are embedded in the aft part of the airframe to suction the turbulent boundary layer developed on the front part of the airframe surface. This removes velocity deficit in the wake region with accelerated exhaust from the engine, which eventually reduces aerodynamic drag. In addition, it is reported that the propulsion performance may be improved by suctioning air flow slowed by wall friction near the airframe [1, 2, 3].

Although BLI is not quite a new idea as it was originally proposed in 1940's, now it draws much attention from many research institutes that apply BLI propulsion systems in the future aircraft design of low-carbon and low-noise concepts [4, 5]. In the view point of noise reduction design, the BLI engine configuration can attain better noise shielding effects given by airframe itself [6]. In particular, engine fan noise is a major noise source of modern commercial aircraft with turbo-fan engines in the takeoff and landing process. To lower the noise level perceived at ground, the airframe noise shielding technique can be very effective by installing engine nacelles above the aft fuselage. However, as the BLI engine suctions turbulent boundary layer that contains very strong vortical fluctuations, its fan noise level can be rather increased by up to 10dB due to the interference between fan blades and turbulent eddies [6]. Therefore, the fan-noise propagation characteristics on the BLI engine must be evaluated with great care in a low-noise design process of aircraft.



Figure 1 – Wide fuselage fuel-efficient, low-noise conceptual aircraft, HELNA, in the baseline configuration.

In JAXA, we also have been conducting extensive research on fuel-efficient, low-noise aircraft design by proposing a midsize conceptual aircraft as the technology reference model, referred to as High Efficiency and Low Noise Aircraft (HELNA), shown in Figure 1. In its original low-noise design, engine nacelles are mounted on the rear part of the double bubble, wide fuselage that increases noise shielding efficiency. Also, a very peculiar, U-shaped tail wing is employed to shield noise emitted from the bypass fan exhaust. On the evaluation of engine fan-noise, here we focus on the propagation of narrow-band noise at specific frequencies. The fundamental frequency of fan noise is given as the blade-passing frequency of the rotor. The present authors examined HELNA's fannoise shielding characteristics in our previous study for the primary tone propagating in a stationary medium [7].

In the present study, our aim is to computationally analyze the fan-noise propagation of JAXA's aircraft model, HELNA in a takeoff condition. In the original design, two engine nacelles are mounted with pylons on the rear fuselage. We refer to this original design as baseline model. We also look into the BLI engine configuration of HELNA by removing pylons from the original design, without changing the streamwise positions of engines. Although the nacelle geometry is the same as that of the baseline model, the engines are embedded by introducing an air-intake slope ahead of the engine nacelle. Their external views are compared in Figure 2. The noise propagation is solved volumetrically in a takeoff condition with background flow, by employing the convected acoustic wave equation that can simulate local convection effects on acoustic propagation [8]. We only examine the acoustic behavior of a single frequency of the primary fan-noise peak, solved in the frequency domain. To reproduce fan noise, modal noise source is imposed on the fan surface of nacelles by using the spinning mode approach [9, 10, 11, 12]. Noise propagation characteristics are evaluated with near-field acoustic solutions, and also with far-field prediction results. Once a near-field acoustic field is obtained, farfield behavior is evaluated by the Ffowcs Williams and Hawkings (FW-H) integral approach. By defining far-field observer locations on a sphere, the spherical directivity patterns are visualized, and compared quantitatively between the two engine geometrical configurations.

# 2. Numerical Methodology

## 2.1 Governing Equations

In this section, the numerical methodology to solve the acoustic wave propagation is briefly explained. To three-dimensionally simulate the propagation of acoustic waves including the effects of reflection and diffraction on obstacles, and advection of background flow, the time-advancing approach using a linearized set of either Euler or Naiver-Stokes equations has been attracting interests in the field of computational aeroacoustics (CAA). However, the time step size  $\Delta t$  is limited by explicit time advancement schemes usually adopted in a high-order CAA approach. On the other hand, the convected

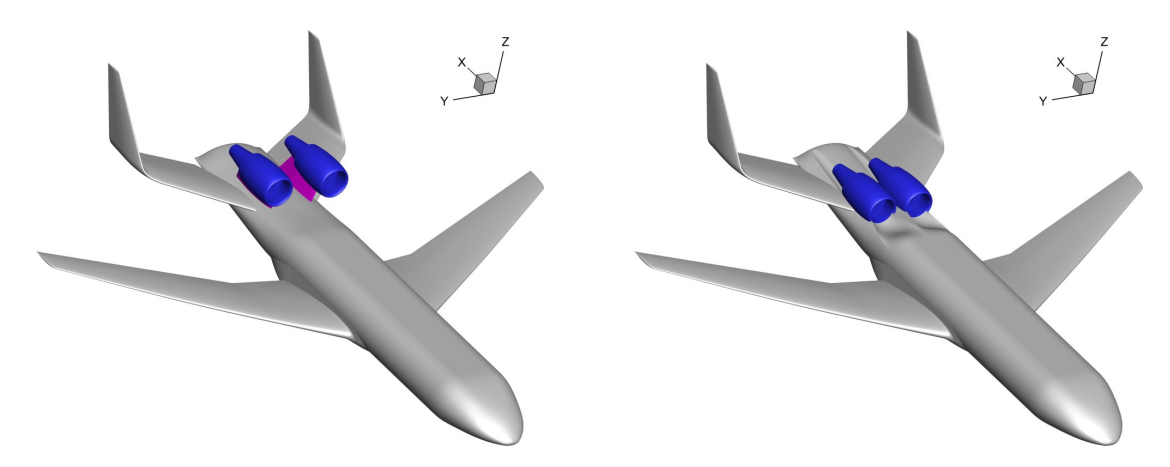


Figure 2 – HELNA models examined for fan-noise shielding: original baseline configuration (left); modified design for BLI engine configuration (right).

wave equation does not have restrictions on the time step size if solved in the frequency domain. In the time domain, the convected wave equation can be written for acoustic velocity potential  $\phi$  as [13, 14]:

$$\left[\frac{1}{\rho}\nabla \cdot (\rho\nabla) - \frac{D}{Dt}\left(\frac{1}{c^2}\frac{D}{Dt}\right)\right]\phi = S \tag{1}$$

where c is local acoustic velocity,  $D/Dt = \partial/\partial t + \vec{u} \cdot \nabla$  is Lagrangian time derivative on fluid particle motion at velocity  $\vec{u}$ ,  $\rho$  is density, and S is volumetric acoustic source. Once solving the equation for  $\phi$ , acoustic pressure p' is obtained from the Bernoulli equation for unsteady, compressible flow:

$$p' = -\rho \frac{D\phi}{Dt} \tag{2}$$

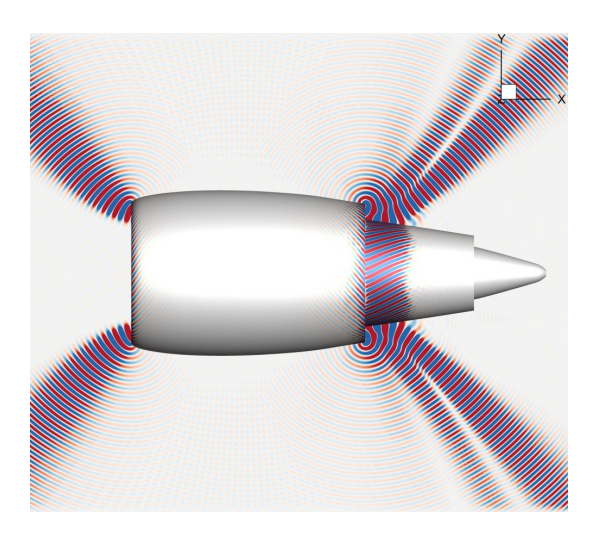
To solve for the particular frequencies of fan noise, we apply the Fourier transformation to the time-domain wave equation, Equation (1). Let  $\widehat{f}$  be the Fourier mode of generic function f for the frequency  $\omega$ . Then its single mode  $f_{\omega}$  can be written in time domain as:  $f_{\omega}(\vec{x},t) = e^{-i\omega t} \widehat{f}(\vec{x})$ . On the frequency  $\omega$ , the frequency-domain formulation of the wave equation can be expressed as:

$$\left[\frac{1}{\rho}\nabla \cdot (\rho\nabla) - \vec{u} \cdot \nabla \left(\frac{1}{c^2}\vec{u} \cdot \nabla\right) + \left(\frac{\omega}{c}\right)^2 + i\omega\left(\vec{u} \cdot \nabla \frac{1}{c^2} + \frac{1}{c^2}\vec{u} \cdot \nabla\right)\right]\widehat{\phi} = \widehat{S}$$
(3)

Equation (3) is often solved by the finite element method. In this study, however, the frequency-domain equation is solved with sixth-order finite difference compact schemes [15, 16] on the Cartesian grid with a hierarchical refinement technique. Grid refinement level is fixed within each rectangular numerical block, discretized by homogeneous grid spacing in each direction. Across the interface of different grid refinement levels, the fifth-order accurate Lagrange interpolation is utilized to smoothly connect acoustic velocity potential  $\hat{\phi}$ . To represent impermeable wall boundaries, an immersed boundary approach is employed. The matrix inversion of the discretized frequency-domain equation is performed by the GMRES iterative technique [17]. At outer boundaries, a non-reflecting boundary condition is implemented with a sponge layer approach that forces out-going waves to decay. Usually, the layer thickness of two or three wavelengths is adequate to remove unwanted reflection. Details of numerical implementations as well as several benchmark studies are summarized in our previous work [8].

# 2.2 Fan Noise Source: Spinning Mode

In this study, we focus on the narrow-band characteristics of the engine fan noise. To reproduce fan noise radiated from the engine nacelle, we employ the spinning mode approach configured for the nacelle with cones [10]. Any spin-like patterns in cylindrical coordinates can be decomposed by Fourier-Bessel series. Modal acoustic fluctuations are imposed on control surfaces defined on an



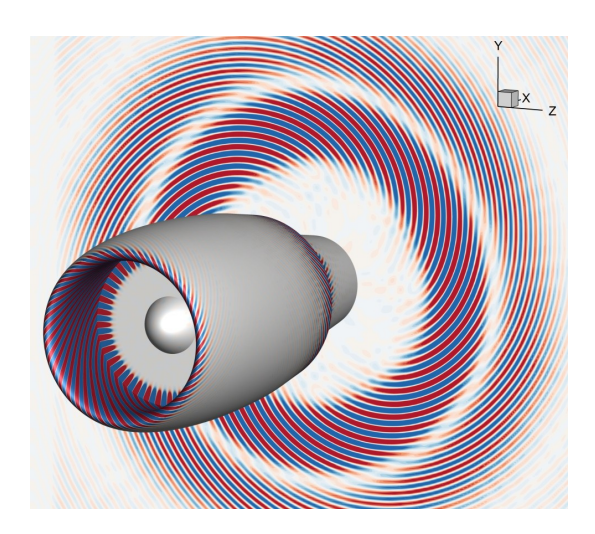


Figure 3 – Instantaneous acoustic pressure distributions at 2.5kHz around the CF6 engine nacelle placed in stationary air: lateral view (left); front view (right). The color range indicates  $\pm 0.01$  from blue to red.

engine nacelle. As the nacelle geometry, we employ General Electric CF6-80C2 in both the baseline and the BLI engine configurations. The engine has been adopted by many commercial and military aircraft, including Boeing B767-200ER. Here we approximate the fan noise using a single Fourier mode, m = 38, which is equal to the number of rotor blades of the CF6 engine. In the radial direction, the lowest order Bessel mode is utilized, reaching the maximum at the outer tip of the fan. This maximum amplitude is used to normalize acoustic pressure, shown in the rest of the paper. The airintake diameter is given as 2.3[m]. Here we assume the blade-passing frequency is given as 2500Hz, which corresponds to the maximum rotational velocity required for a takeoff of a midsize aircraft.

Figure 3 shows the fan-noise propagation patterns of an isolated nacelle in stationary air at 2500Hz, taken from our previous result [7]. In a standard air state, one acoustic wavelength is estimated as 0.14 [m] at this frequency. In the present single nacelle case, total number of Cartesian numerical cells is  $6.6 \times 10^7$ . As can bee seen from the figure, the emitted tonal noise shows peculiar directivity propagating in the diagonal directions toward upstream from the front fan surface, captured in the lateral view. In the front view, the spinning pattern can be recognized in the right-hand screw direction in the upstream direction. In the downstream direction, the noise is also emitted from the bypass fan exhaust, spinning in the opposite direction.

## 3. Numerical Conditions

### 3.1 Computational Domain

The size of the present airframe model, HELNA, is: 48.2 [m] in length (x), 47.6 [m] in width (y), and 10.4 [m] in height (z), which corresponds to a common midsize commercial aircraft. The computational domain for acoustic propagation is given as a cuboid of the size: 53 [m]  $\times$  52 [m]  $\times$  15 [m] including buffer layers to damp the acoustic waves toward outer boundaries, as shown in Figure 4. The number of the present Cartesian numerical cells with 1-step hierarchical refinement is  $5.0 \times 10^9$  for the entire aircraft. The finer cell width corresponds to 12 points per wavelength (PPW) for the acoustic wave traveling in stationary medium at 2500Hz near the airframe surface. The present grid resolution is supposed to be adequate as our benchmark case of 5 PPW is accurate enough for acoustic scattering on a circular cylinder [8].

# 3.2 Background Flow

To consider the convection effect on the acoustic propagation in the flight condition, first the flow field is solved by an unstructured-grid Reynolds-averaged Navier-Stokes equation (RANS) solver using

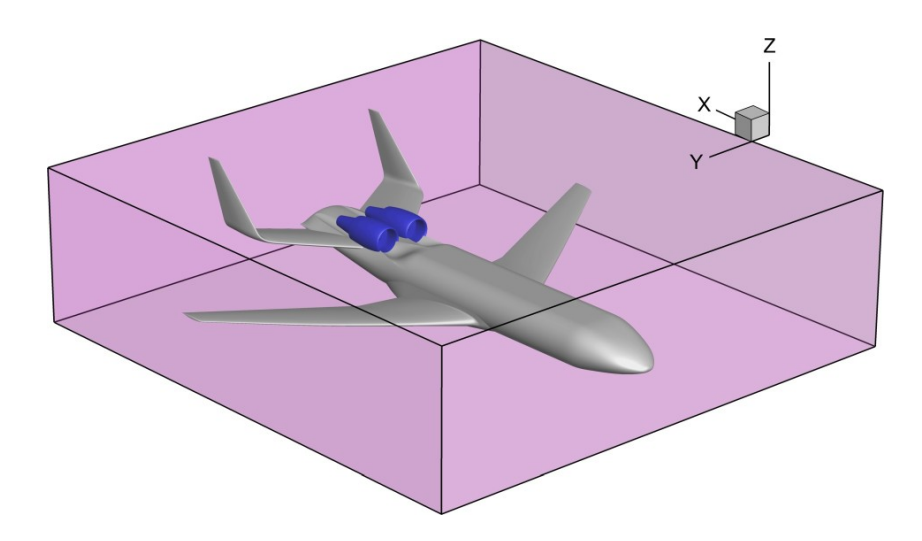


Figure 4 – The acoustics computational box containing entire BLI-HELNA airframe.

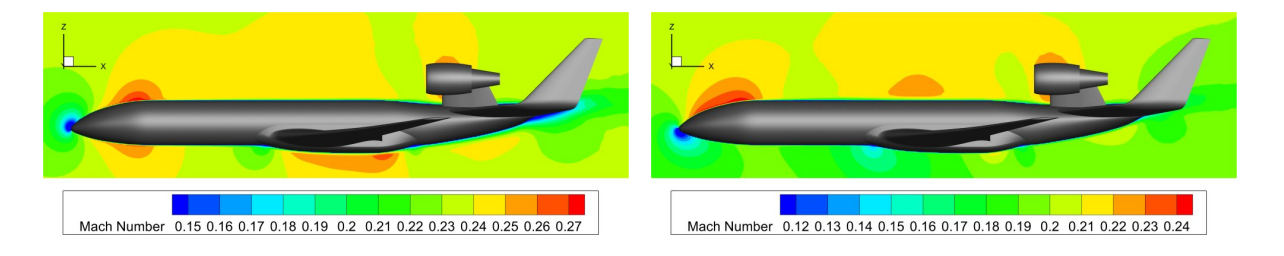


Figure 5 – Mach contours on the center vertical plane of the fuselage for the baseline model:  $\alpha = 0^{\circ}$  (left) and  $\alpha = 16^{\circ}$  (right).

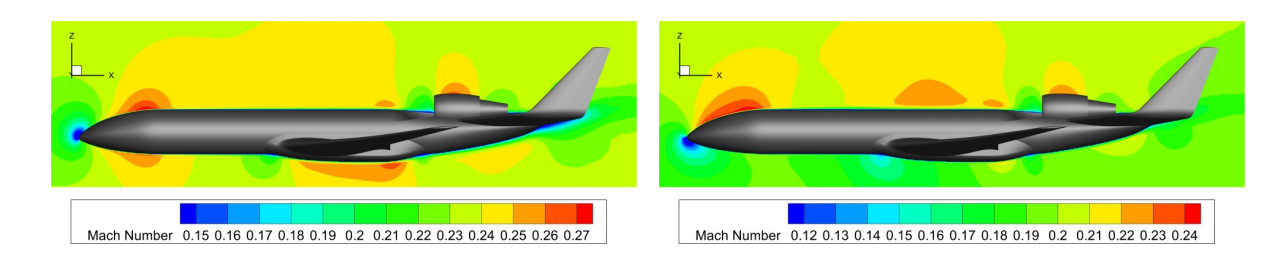


Figure 6 – Mach contours on the center vertical plane of the fuselage for the BLI model:  $\alpha=0^{\circ}$  (left) and  $\alpha=16^{\circ}$  (right).

the Spalart-Allmaras turbulence model. Here, the inflow Mach number  $M_{\infty}$  is assumed to be 0.2. The Reynolds number based on HELNA's wingspan reaches  $2.2 \times 10^8$ . We chose two different angles of attack:  $\alpha = 0^{\circ}$  and  $16^{\circ}$ . The latter angle is intended to simulate takeoff configurations. The zero-incidence case is also conducted to examine the effect of inclined flow angle of the takeoff condition on the acoustic propagation. The flow fields obtained on unstructured grid are projected onto the Cartesian grid by linear interpolation for the calculation of acoustic propagation, shown in Figures 5 and 6. The engine nacelle is regarded to be a flow-through geometry here. Therefore, the velocity deficit does exist behind the exhaust for the BLI configuration in the present computations. Besides, on the upper side of the aft-fuselage, an air-intake slope is imposed ahead of the nacelles, where the flow is decelerated. It slightly decreases lift forces compared with the baseline design, although we rather focus on its effects on acoustic propagation in the present study.

# 4. Results

In this section, the results of fan-noise scattering and propagation are presented and discussed on the baseline and BLI aircraft models. The present 5 billion-cell computations for volumetric acoustic propagation were performed on JAXA Supercomputer System JSS3, by using 300 A64FX processors. The wall clock time required for the convergence in each computation case is 30–40 hours.

# 4.1 Instantaneous Acoustic Field

Here instantaneous sound pressure distributions are presented. However, as the pressure is given in the frequency-domain representation in complex values, its real part is shown as the instantaneous solution at t=0. In Figures 7 and 8, the instantaneous fan-noise distribution is shown in a diagonal overhead view, with cuboid control surfaces that enclose the aircraft models. The cuboid is a part of the computational domain by eliminating sponge layers set near the outer boundaries. Also these cuboid surfaces are utilized as sound sources for the far-field sound estimation using the FW-H equation, shown in the following section. In all the cases, as two engine fans settled on the aftfuselage are both spinning in the same direction, the solutions are not symmetric on the center vertical plane. The rear part of the upper fuselage surface is exposed strongly to the fan noise, as well as the inner side of the U-shaped tail wing. The downward noise seems to be shielded guite effectively by these airframe surfaces. Toward the upstream direction, the main wings also work as noise masking. In the present spinning direction, the left wing is more exposed to the fan noise. Also, by adding angle of attack, exposed area on the main wings is somewhat decreased. The introduction of the present BLI design, however, shows a rather significant impact on the fan-noise shielding. On the bottom cuboid surface of the BLI model, noise exposed area is apparently decreased. Also on the aft-fuselage, the noise exposed area is only limited near the slope ahead of the BLI engines in the upstream direction. The BLI configurations introduced on the upper side of the aft-fuselage effectively reduce the noise that leaks in the downward direction.

The fan-noise reflected on the fuselage may receive more influence by the velocity field near the airframe, altered from uniform flow. In particular, the intake slope introduced on the rear fuselage ahead of the nacelles slows down the flow, and thus alters the reflection patterns. Figures 9 and 10 compare the lateral views of noise propagation. In the baseline configurations shown in Figure 9, the fan noise seems simply pushed back by the uniform flow. The added angle of attack slightly sets back the noise propagation region in the downstream direction. In Figure 9 of the BLI case, however, the noise reflection patterns are a little more complicated. Because of the slowed down region above the fuselage in the inclined uniform flow case, the reflected noise reaches a more upstream region. Nonetheless, in both angles of attack, the BLI case shows a greater amplitude of noise interference in the upper direction, which is the evidence of better shielding capability against downward acoustic propagation.

# 4.2 Far-field Noise Directivity

Here the fan-noise shielding capability is assessed with the far-field noise directivity. The far-field noise is calculated by the FW-H integral approach modified for frequency domain [18, 19, 20]. In

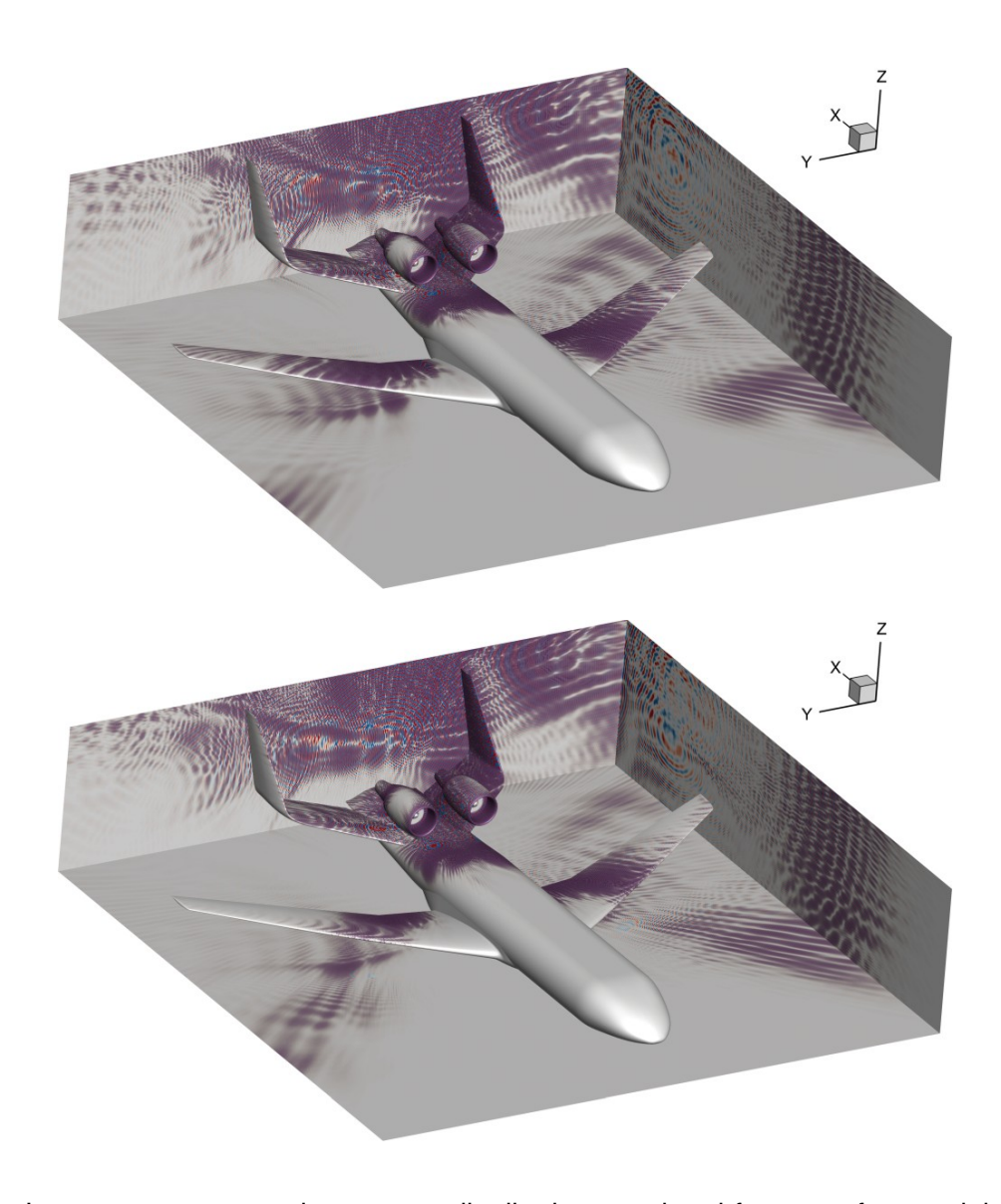


Figure 7 – Instantaneous acoustic pressure distributions on the airframe surface and the cuboid control surface for the baseline model:  $\alpha=0^\circ$  (top) and  $\alpha=16^\circ$  (bottom); the color range indicates  $\pm 0.01$  from blue to red, normalized with the magnitude of spinning-mode source pressure fluctuations given on the nacelle fan surface.

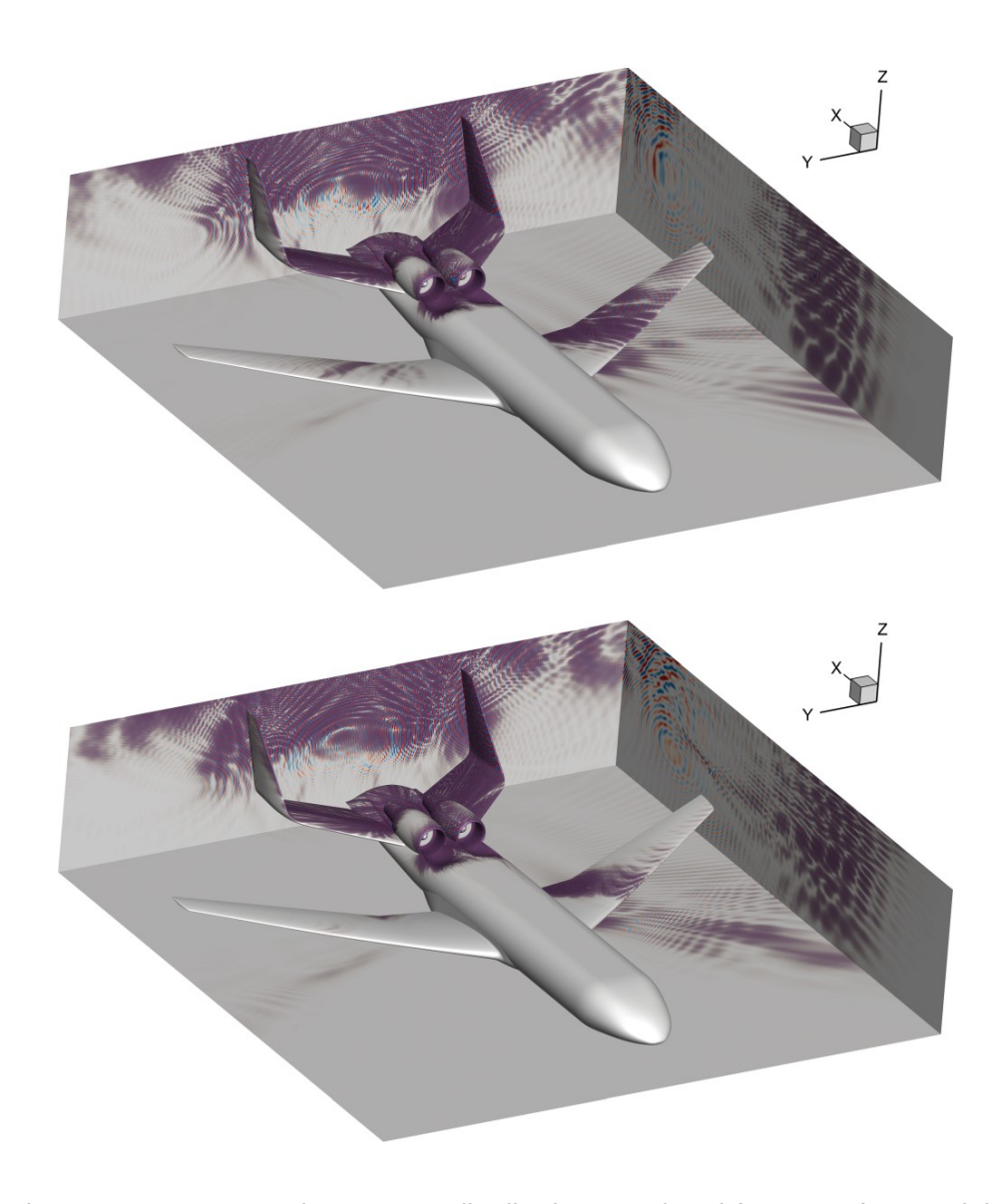


Figure 8 – Instantaneous acoustic pressure distributions on the airframe surface and the cuboid control surface for the BLI model:  $\alpha=0^\circ$  (top) and  $\alpha=16^\circ$  (bottom); the color range indicates  $\pm 0.01$  from blue to red.





Figure 9 – The lateral view of instantaneous acoustic pressure distributions on the rear part of the airframe surface and the center vertical plane for the baseline model:  $\alpha=0^{\circ}$  (left) and  $\alpha=16^{\circ}$  (right); the color range indicates  $\pm 0.01$  from blue to red.





Figure 10 – The lateral view of instantaneous acoustic pressure distributions on the rear part of the airframe surface and the center vertical plane for the BLI model:  $\alpha=0^{\circ}$  (left) and  $\alpha=16^{\circ}$  (right); the color range indicates  $\pm 0.01$  from blue to red.

this study, observer locations are defined on a sphere of the radius 500 [m] from the tail of the aircraft models. The observer sphere is discretized in spherical coordinates of  $360 \times 180$  points in the longitude and the latitude directions, respectively.

Figures 11 and 12 present the root-mean-squared (RMS) acoustic pressure fluctuation distributions on the observer sphere viewed from the top to examine the fan-noise propagation and reflection in the upper direction. The RMS values are normalized with the pressure-fluctuation maximum value on the fan surface. As also indicated in the instantaneous results, the magnitude of reflected pressure in the BLI case is obviously greater than that of the baseline case. Each RMS sound pressure distribution on the hemisphere shows the peculiar directivity patterns of engine fan noise emitted from the present nacelle geometry.

The noise shielding capability is better understood by examining the lower-half of the noise sphere. Figures 13 and 14 present the observer sphere viewed from the bottom. Now the contour range is one digit smaller than the upper hemisphere visualization, as the present low-noise configurations successfully minimize the noise recognition level in the lower direction. However, the BLI design significantly decreases the noise leakage. Noise exposed area in the BLI case is even smaller than the baseline model, as also visualized in the instantaneous results. In the present engine-fan spinning direction, the peak region exposed to the fan noise arises in the left front direction. Other than this specific direction, the BLI configurations quite effectively shield the downward noise propagation.

## 5. Conclusions

In this study, the noise shielding capability of low-noise concept midsize aircraft designs is investigated numerically. In the baseline model design, two engine nacelles are mounted with pylons on the rear part of a wide body attached with a large U-shaped tail wing. The other design introduces the BLI concept by embedding the engine nacelles on the aft fuselage with air-intake slope. The acoustic propagation is computed volumetrically by solving the convected wave equation with inhomogeneous flow field. The fan noise is modeled with a spinning mode, whose target frequency is chosen to be 2500Hz at takeoff operation. The background flow field is obtained by a RANS solver in advance, for inflow Mach number M=0.2, and the angle of attack  $\alpha=0^\circ$  and  $\alpha=16^\circ$ . To resolve acoustic

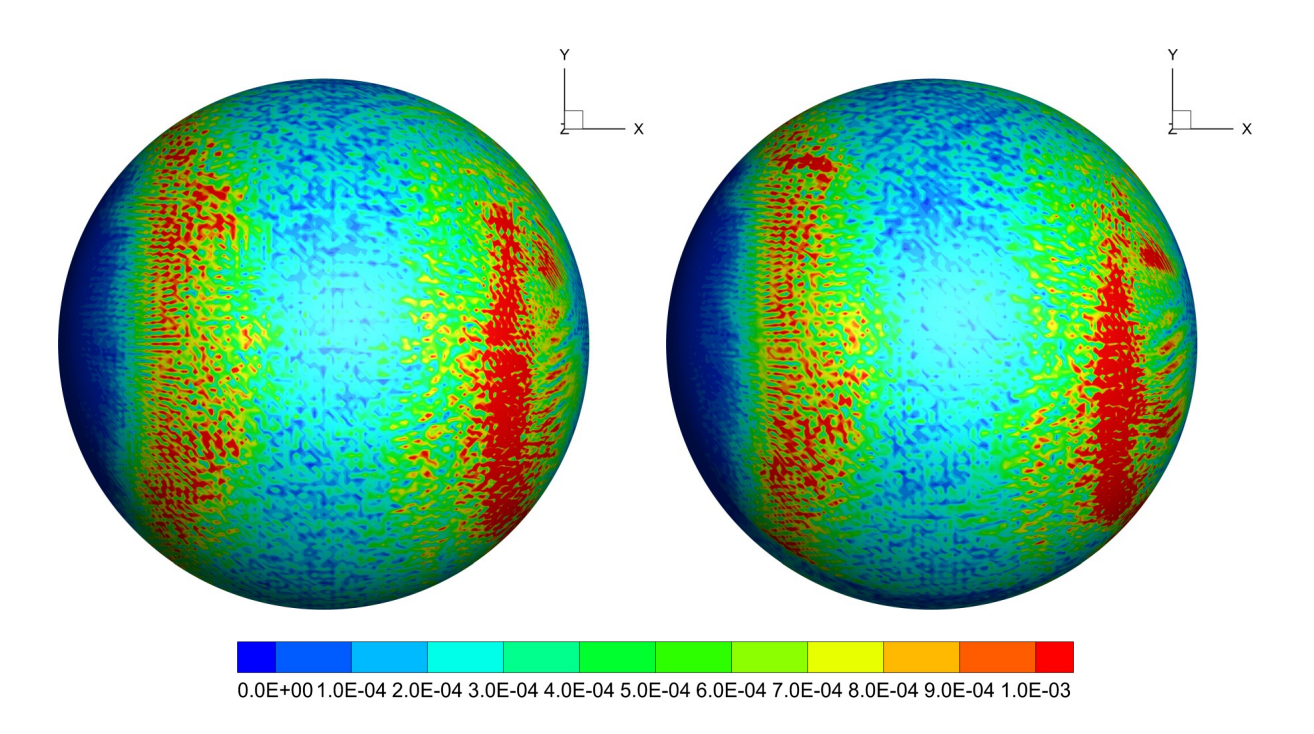


Figure 11 – The upper noise hemisphere at r=500 [m] for the baseline model:  $\alpha=0^\circ$  (left) and  $\alpha=16^\circ$  (right).

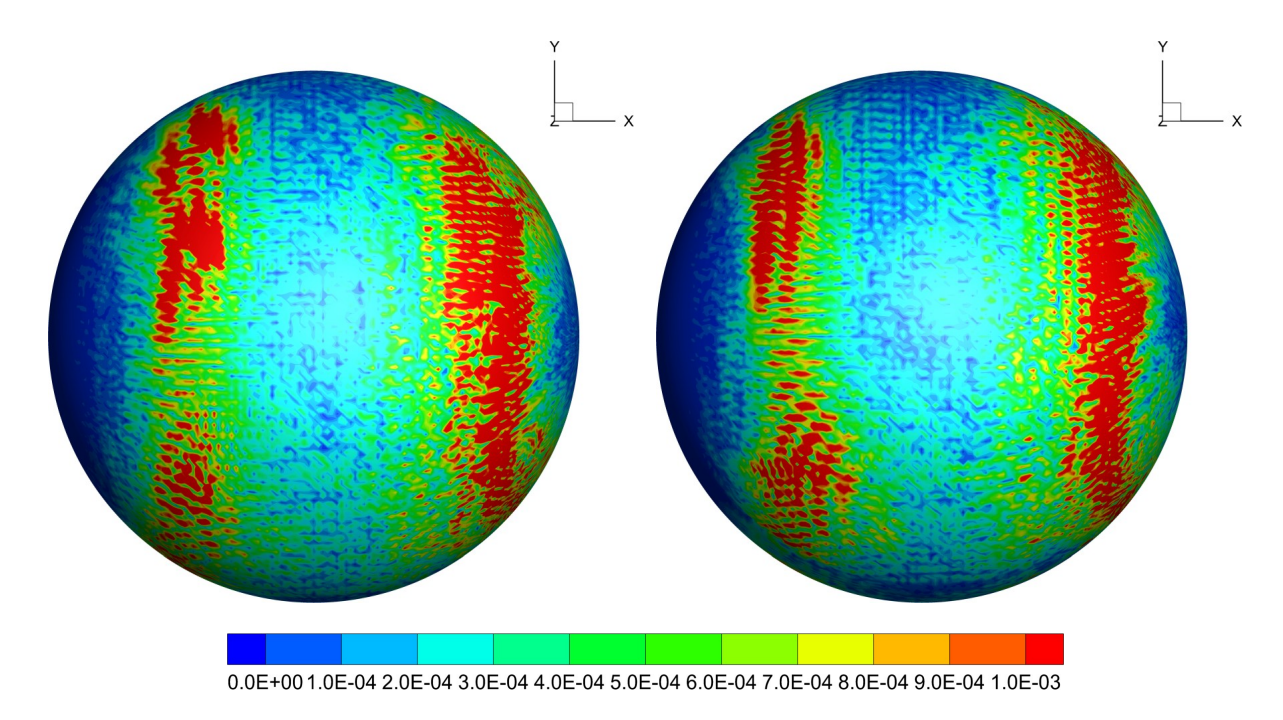


Figure 12 – The upper noise hemisphere at r=500 [m] for the BLI model:  $\alpha=0^\circ$  (left) and  $\alpha=16^\circ$  (right).

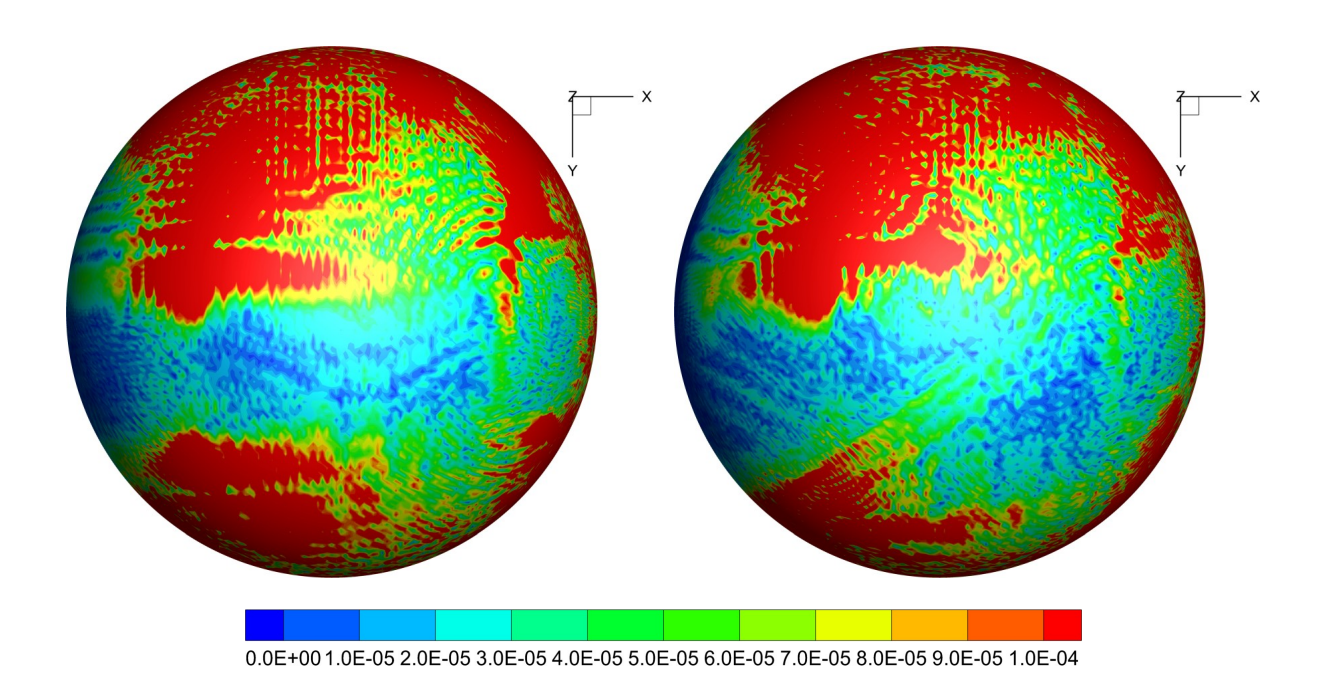


Figure 13 – The lower noise hemisphere at r=500 [m] for the baseline model:  $\alpha=0^\circ$  (left) and  $\alpha=16^\circ$  (right).

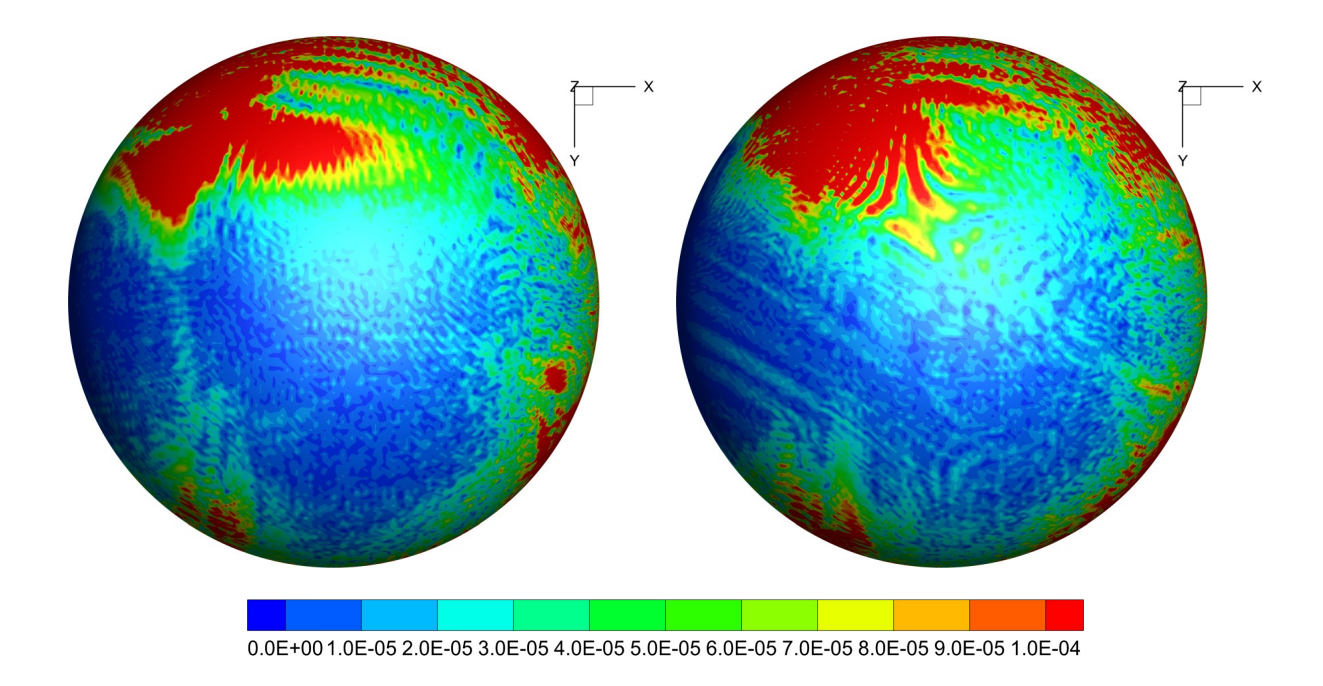


Figure 14 – The lower noise hemisphere at r=500 [m] for the BLI model:  $\alpha=0$ ° (left) and  $\alpha=16$ ° (right).

waves traveling around the present midsize aircraft, 5 billion Cartesian numerical cells are imposed in the cuboid computational domain, while the surface of aircraft models is extracted by an immersed boundary approach.

To evaluate acoustic results, near-field instantaneous acoustic pressure, as well as far-field distributions, are examined. Far-field results are obtained with the FW-H surface integrals. In the instantaneous results, the BLI case shows better capability to suppress the downward noise, although both aircraft models successfully prevent the downward noise from being perceived at ground by noise shielding airframe designs including tail and main wings. More quantitatively, the noise shielding capability is compared by using the FW-H far-field results, evaluated on a noise sphere of the radius 500 [m]. The BLI case shows stronger reflection in the upper direction, and therefore drastically reduces the noise leakage visualized in the lower observer hemisphere.

## 6. Contact Author Email Address

The contact author email address is: ikeda.tomoaki@jaxa.jp

# 7. Copyright Statement

The authors confirm that they, and/or their company or organization, hold copyright on all of the original material included in this paper. The authors also confirm that they have obtained permission, from the copyright holder of any third party material included in this paper, to publish it as part of their paper. The authors confirm that they give permission, or have obtained permission from the copyright holder of this paper, for the publication and distribution of this paper as part of the ICAS proceedings or as individual off-prints from the proceedings.

# References

- [1] B. Blumenthal, A. Elmiligui, K. Geiselhart, R. Campbell, M. Maughmer, and S. Schmitz. Computational investigation of a boundary-layer-ingestion propulsion system. *J. Aircraft*, Vol. 55, No. 3, pp. 1141–1153, 2018.
- [2] M. Drela. Power balance in aerodynamic flows. AIAA J., Vol. 47, No. 7, pp. 1761–1771, 2009.
- [3] N. Moirou, D. Sanders, and P. Laskaridis. Advancements and prospects of boundary layer ingestion propulsion concepts. *Progress in Aerospace Sciences*, Vol. 138, No. 133897, 2023.
- [4] Jim Banke. Beauty of future airplanes is more than skin deep. https://www.nasa.gov/aeronautics/future-airplanes-beauty-more-skin-deep/
- [5] L. Wiart, O. Atinault, B. Paluch, D. Hue, and R. Grenon. Development of NOVA aircraft configurations for large engine integration studies. *AIAA Paper 2015-2254*, 2015.
- [6] I. Clark, R. Thomas, and Y. Guo. Aircraft system noise of the NASA D8 subsonic transport concept. *J. Aircraft*, Vol. 58, No. 5, pp. 1106–1120, 2021.
- [7] T. Ikeda, R. Furuya, and M. Murayama. On the fan-noise shielding effect of fuselage mounted engines. In APISAT 2022: Asia-Pacific International Symposium on Aerospace Technology, Niigata, Japan, October 2022.
- [8] T. Ikeda. Acoustic propagation prediction using the inhomogeneous wave equation on the Cartesian grid. In APISAT 2019: Asia-Pacific International Symposium on Aerospace Technology, pp. 530–540, Gold Coast, Austraria, December 2019.
- [9] G. F. Homicz and J. A. Lordi. A note on the radiative directivity patterns of duct acoustic modes. *J. Sound Vib.*, Vol. 41, No. 3, pp. 283–290, 1975.
- [10] X. Huang, X. Chen, Z. Ma, and X. Zhang. Efficient computation of spinning modal radiation through an engine bypass duct. *AIAA J.*, Vol. 46, No. 6, pp. 1413–1423, 2008.

- [11] S. Redonnet and Y. Druon. Computational aeroacoustics of aft fan noises characterizing a realistic coaxial engine. *AIAA J.*, Vol. 50, No. 5, pp. 1029–1046, 2012.
- [12] X. Zhang, X. X. Chen, C. L. Morfey, and P. A. Nelson. Computation of spinning modal radiation from an unflanged duct. *AIAA J.*, Vol. 42, No. 9, pp. 1795–1801, 2004.
- [13] R. Ewert and W. Schröder. Acoustic perturbation equations based on flow decomposition via source filtering. *J. Comput. Phys.*, Vol. 188, pp. 365–398, 2003.
- [14] A. D. Pierce. Wave equation for sound in fluids with unsteady inhomogeneous flow. *J. Acoust. Soc. Am.*, Vol. 87, No. 6, pp. 2292–2299, 1990.
- [15] I. Harari and E. Turkel. Accurate finite difference methods for time-harmonic wave propagation. *J. Comput. Phys.*, Vol. 119, pp. 252–270, 1995.
- [16] S. K. Lele. Compact finite difference schemes with spectral-like resolution. *J. Comput. Phys.*, Vol. 103, No. 1, pp. 16–42, 1992.
- [17] Y. Saad. *Iterative methods for sparse linear systems*. Society for industrial and applied mathematics, 2nd edition, 2003.
- [18] J. E. Ffowcs Williams and D. L. Hawkings. Sound generation by turbulence and surfaces in arbitrary motion. *Phil. Trans. Roy. Soc. A*, Vol. 264, No. 1151, pp. 321–342, 1969.
- [19] D. P. Lockard. A comparison of FW-H solvers for airframe noise applications. *AIAA Paper 2002-2580*, 2002.
- [20] C. Weckmüller, S. Guérin, J. Wellner, and U. Michel. FW-H formulation for the convective wave equation and permeable data surface. *AIAA Paper 2010-3710*, 2010.